



ELSEVIER

Available online at [www.sciencedirect.com](http://www.sciencedirect.com)

SCIENCE @ DIRECT®

Computers and Mathematics with Applications 51 (2006) 1269–1282

---

An International Journal  
**computers &  
mathematics**  
with applications

---

[www.elsevier.com/locate/camwa](http://www.elsevier.com/locate/camwa)

# Meshfree Explicit Local Radial Basis Function Collocation Method for Diffusion Problems

B. ŠARLER AND R. VERTNIK

Laboratory for Multiphase Processes

Nova Gorica Polytechnic, Vipavska 13

SI-5000, Nova Gorica, Slovenia

&lt;bozidar.sarler&gt;&lt;robert.vertnik&gt;@p-ng.si

**Abstract**—This paper formulates a simple explicit local version of the classical meshless radial basis function collocation (Kansa) method. The formulation copes with the diffusion equation, applicable in the solution of a broad spectrum of scientific and engineering problems. The method is structured on multiquadrics radial basis functions. **Instead of global, the collocation is made locally over a set of overlapping domains of influence and the time-stepping is performed in an explicit way. Only small systems of linear equations with the dimension of the number of nodes included in the domain of influence have to be solved for each node.** The computational effort thus grows roughly linearly with the number of the nodes. The developed approach thus overcomes the principal large-scale problem bottleneck of the original Kansa method. Two test cases are elaborated. The first is the boundary value problem (NAFEMS test) associated with the steady temperature field with simultaneous involvement of the Dirichlet, Neumann and Robin boundary conditions on a rectangle. The second is the initial value problem, associated with the Dirichlet jump problem on a square. The accuracy of the method is assessed in terms of the average and maximum errors with respect to the density of nodes, number of nodes in the domain of influence, multiquadrics free parameter, and timestep length on uniform and nonuniform node arrangements. The developed meshless method outperforms the classical finite difference method in terms of accuracy in all situations except immediately after the Dirichlet jump where the approximation properties appear similar. © 2006 Elsevier Ltd. All rights reserved.

## 1. INTRODUCTION

The problems in science and engineering are usually reduced to a set of coupled partial differential equations. It is not easy to obtain their analytical solution, particularly in nonlinear and complex-shaped cases, and discrete approximate methods have to be employed accordingly. The finite-difference method (FDM), the finite-element method (FEM), and the boundary-element method (BEM) are most widely used among them at the present. Despite the powerful features of these methods, there are often substantial difficulties in their application to realistic, geometrically complex, three-dimensional transient situations with moving and/or deforming boundaries. A common complication in the mentioned methods is the need to create a polygonisation, either in the domain and/or on its boundary. This type of (re)meshing is often the most time-consuming part of the solution process and is far from being fully automated.

---

The authors acknowledge the support of the Slovenian Ministry for High Education, Science and Technology in the framework of the Grant J2-640-1540-04.

0898-1221/06/\$ - see front matter © 2006 Elsevier Ltd. All rights reserved.  
doi:10.1016/j.camwa.2006.04.013

Typeset by  $\mathcal{A}\mathcal{M}\mathcal{S}$ -TEX

In recent years, a new class of methods is in development which does not require polygonisation but uses only a set of nodes to approximate the solution. The rapid development of these types of meshfree (meshless, polygon-free) methods and their classification is elaborated in the very recent monographs [1–4]. A broad class of meshfree methods in development today is based on radial basis functions (RBFs) [5]. The RBF collocation method or Kansa method [6] is the simplest of them. This method has been further upgraded to symmetric collocation [7,8], to modified collocation [9] and to indirect collocation [10]. The method has been already used in a broad spectrum of computational fluid dynamics problems [11] such as the solution of Navier-Stokes equations [12] or porous media flow [13] and the solution of solid-liquid phase change problems [14]. In contrast to advantages over mesh generation, all the listed methods unfortunately fail to perform for large problems, because they produce fully populated matrices, sensitive to the choice of the free parameters in RBFs. Sparse matrices can be generated by the introduction of the compactly supported RBFs, and the accuracy of such an approach can be improved by the multilevel technique [15]. One of the possibilities for mitigating the large fully populated matrix problem is to employ the domain decomposition [16]. However, the domain decomposition reintroduces some sort of meshing which is not attractive. The concept of local collocation in the context of an RBF-based solution of the Poisson equation has been introduced in [17,18]. For interpolation of the function value in a certain node the authors use only data in the (neighbouring) nodes that fall into the domain of influence of this node. The procedure results in a matrix that is of the same size as the matrix in the original Kansa method, however it is sparse. Circular domains of influence have been used in [17] and stencil-shaped domains in [18]. In [17], the one-dimensional and two-dimensional Poisson equation has been solved by using multiquadrics and inverse multiquadrics RBFs with a detailed analysis of the influence of the free parameter on the results. In [18], a class of linear and nonlinear elasticity problems have been solved with a fixed free parameter. The differential quadrature method that calculates the derivatives of a function by a weighted linear sum of functional values at its neighbouring nodes has been structured with the RBFs in [19]. Despite the local properties, the matrix still has a similar form as in [17,18]. This paper formulates a simple meshfree solution procedure for solving the diffusion equation which overcomes even the solution of the large sparse matrices.

## 2. GOVERNING EQUATIONS

Let us limit our discussion to solution of the heat diffusion equation, defined on a fixed domain  $\Omega$  with boundary  $\Gamma$

$$\rho c \frac{\partial}{\partial t} T = \nabla \cdot (k \nabla T), \quad (1)$$

with  $\rho$ ,  $c$ ,  $k$ ,  $T$ ,  $t$  standing for density, specific heat, thermal conductivity, temperature, and time. The material properties  $\rho$ ,  $c$ ,  $k$  may depend on the position and temperature, i.e., the problem might be inhomogeneous and nonlinear. The solution of the governing equation for the temperature at the final time  $t_0 + \Delta t$  is sought, where  $t_0$  represents the initial time and  $\Delta t$  the positive time increment. The solution is constructed by the initial and boundary conditions that follow. The initial value of the temperature  $T(\mathbf{p}, t)$  at a point with position vector  $\mathbf{p}$  and time  $t_0$  is defined through the known function  $T_0$

$$T(\mathbf{p}, t_0) = T_0(\mathbf{p}); \quad \mathbf{p} \in \Omega + \Gamma. \quad (2)$$

The boundary  $\Gamma$  is divided into not necessarily connected parts  $\Gamma = \Gamma^D \cup \Gamma^N \cup \Gamma^R$  with Dirichlet, Neumann, and Robin type boundary conditions, respectively. At the boundary point  $\mathbf{p}$  with normal  $\mathbf{n}_\Gamma$  and time  $t_0 \leq t \leq t_0 + \Delta t$ , these boundary conditions are defined through known

functions  $T_\Gamma^D, T_\Gamma^N, T_\Gamma^R, T_{\Gamma^{\text{ref}}}^R$

$$T = T_\Gamma^D; \quad \mathbf{p} \in \Gamma^D, \quad (3)$$

$$\frac{\partial}{\partial n_\Gamma} T = T_\Gamma^N; \quad \mathbf{p} \in \Gamma^N, \quad (4)$$

$$\frac{\partial}{\partial n_\Gamma} T = T_\Gamma^R (T - T_{\Gamma^{\text{ref}}}^R); \quad \mathbf{p} \in \Gamma^R. \quad (5)$$

### 3. SOLUTION PROCEDURE

The representation of temperature over a set of  ${}_lN$  arbitrarily spaced nodes  ${}_l\mathbf{p}_n$ ;  $n = 1, 2, \dots, {}_lN$  is made in the following way:

$$T(\mathbf{p}) \approx \sum_{k=1}^{{}_lK} {}_l\psi_k(\mathbf{p}) {}_l\alpha_k, \quad (6)$$

where  ${}_l\psi_k$  stands for the shape functions,  ${}_l\alpha_k$  for the coefficients of the shape functions, and  ${}_lK$  represents the number of the shape functions. The left lower index on entries of expression (6) represents the domain of influence (subdomain)  ${}_l\omega$  on which the coefficients  ${}_l\alpha_k$  are determined. The domains of influence  ${}_l\omega$  can in general be overlapping or nonoverlapping. Each of the domains of influence  ${}_l\omega$  includes  ${}_lN$  nodes of which  ${}_lN_\Omega$  can in general be in the domain and  ${}_lN_\Gamma$  on the boundary, i.e.,  ${}_lN = {}_lN_\Omega + {}_lN_\Gamma$ . The domain of influence of the node  ${}_l\mathbf{p}$  is defined with the nodes having the nearest  ${}_lN - 1$  distances to the node  ${}_l\mathbf{p}$ . The five node  ${}_lN = 5$  and nine node supports  ${}_lN = 9$  are used in this paper. The coefficients can be calculated from the subdomain nodes in two distinct ways. The first way is collocation (interpolation) and the second way is approximation by the least squares method. Only the simpler collocation version for calculation of the coefficients is considered in this text. Let us assume the known function values  ${}_lT_n$  in the nodes  ${}_l\mathbf{p}_n$  of the subdomain  ${}_l\omega$ . The collocation implies

$$T({}_l\mathbf{p}_n) = \sum_{k=1}^{{}_lN} {}_l\psi_k({}_l\mathbf{p}_n) {}_l\alpha_k. \quad (7)$$

For the coefficients to be computable, the number of the shape functions has to match the number of the collocation points  ${}_lK = {}_lN$ , and the collocation matrix has to be nonsingular. The system of equations (7) can be written in a matrix-vector notation

$${}_l\psi {}_l\alpha = {}_l\mathbf{T}; \quad {}_l\psi_{kn} = {}_l\psi_k({}_l\mathbf{p}_n), \quad {}_lT_n = T({}_l\mathbf{p}_n). \quad (8)$$

The coefficients  ${}_l\alpha$  can be computed by inverting system (8)

$${}_l\alpha = {}_l\psi^{-1} {}_l\mathbf{T}. \quad (9)$$

By taking into account the expressions for the calculation of the coefficients  ${}_l\alpha$ , the collocation representation of temperature  $T(\mathbf{p})$  on subdomain  ${}_l\omega$  can be expressed as

$$T(\mathbf{p}) \approx \sum_{k=1}^{{}_lN} {}_l\psi_k(\mathbf{p}) \sum_{n=1}^{{}_lN} {}_l\psi_{kn}^{-1} {}_lT_n. \quad (10)$$

Let us introduce a two-dimensional Cartesian coordinate system with base vectors  $\mathbf{i}_\varsigma$ ;  $\varsigma = x, y$  and coordinates  $p_\varsigma$ ;  $\varsigma = x, y$ , i.e.,  $\mathbf{p} = \mathbf{i}_x p_x + \mathbf{i}_y p_y$ . The first partial spatial derivatives of  $T(\mathbf{p})$  on subdomain  ${}_l\omega$  can be expressed as

$$\frac{\partial}{\partial p_\varsigma} T(\mathbf{p}) \approx \sum_{k=1}^{{}_lN} \frac{\partial}{\partial p_\varsigma} {}_l\psi_k(\mathbf{p}) \sum_{n=1}^{{}_lN} {}_l\psi_{kn}^{-1} {}_lT_n; \quad \varsigma = x, y. \quad (11)$$

The second partial spatial derivatives of  $T(\mathbf{p})$  on subdomain  ${}_l\omega$  can be expressed as

$$\frac{\partial^2}{\partial p_\varsigma \partial p_\xi} T(\mathbf{p}) \approx \sum_{k=1}^{iN} \frac{\partial^2}{\partial p_\varsigma \partial p_\xi} {}_l\psi_k(\mathbf{p}) \sum_{n=1}^{iN} {}_l\psi_{kn}^{-1} T_n; \quad \varsigma, \xi = x, y. \quad (12)$$

Radial basis functions [5], such as multiquadrics, can be used for the shape functions

$${}_l\psi_k(\mathbf{p}) = [{}_lr_k^2(\mathbf{p}) + c^2 {}_lr_0^2]^{1/2}; \quad {}_lr_k^2 = (\mathbf{p} - {}_l\mathbf{p}_k) \cdot (\mathbf{p} - {}_l\mathbf{p}_k), \quad (13)$$

where  $c$  represents the dimensionless shape parameter. The scaling parameter  ${}_lr_0^2$  is set to the maximum nodal distance in the domain of influence

$${}_lr_0^2 = \max_l r_m^2({}_l\mathbf{p}_n); \quad m, n = 1, 2, \dots, iN. \quad (14)$$

The explicit values of the involved first and second derivatives of  $\psi_k(\mathbf{p})$  are

$$\frac{\partial}{\partial p_x} {}_l\psi_k(\mathbf{p}) = \frac{p_x - {}_lp_{kx}}{({}_lr_k^2 + c^2 {}_lr_0^2)^{1/2}}, \quad (15)$$

$$\frac{\partial}{\partial p_y} {}_l\psi_k(\mathbf{p}) = \frac{p_y - {}_lp_{ky}}{({}_lr_k^2 + c^2 {}_lr_0^2)^{1/2}}, \quad (16)$$

$$\frac{\partial^2}{\partial p_x^2} {}_l\psi_k(\mathbf{p}) = \frac{(p_y - {}_lp_{ky})^2 + c^2 {}_lr_0^2}{({}_lr_k^2 + c^2 {}_lr_0^2)^{3/2}}, \quad (17)$$

$$\frac{\partial^2}{\partial p_y^2} {}_l\psi_k(\mathbf{p}) = \frac{(p_x - {}_lp_{kx})^2 + c^2 {}_lr_0^2}{({}_lr_k^2 + c^2 {}_lr_0^2)^{3/2}}, \quad (18)$$

$$\frac{\partial^2}{\partial p_x \partial p_y} {}_l\psi_k(\mathbf{p}) = \frac{\partial^2}{\partial p_y \partial p_x} {}_l\psi_k(\mathbf{p}) = \frac{(p_x - {}_lp_{kx})(p_y - {}_lp_{ky})}{({}_lr_k^2 + c^2 {}_lr_0^2)^{3/2}}. \quad (19)$$

What follows elaborates the solution of the heat diffusion equation (1), subject to the initial condition (2), and boundary conditions (3)–(5). The diffusion equation can be transformed into the following expression by taking into account the explicit time discretization:

$$\rho c \frac{\partial T}{\partial t} \approx \frac{\rho_0 c_0 T - \rho_0 c_0 T_0}{\Delta t} = \nabla \cdot (k_0 \nabla T_0). \quad (20)$$

The unknown function value  $T_l$  in domain node  $\mathbf{p}_l$  can be calculated as

$$T_l T_{0l} + \frac{\Delta t}{\rho_{0l} c_{0l}} \nabla \cdot (k_{0l} \nabla T_{0l}) = T_{0l} + \frac{\Delta t}{\rho_{0l} c_{0l}} [\nabla k_{0l} \cdot \nabla T_{0l} + k_{0l} \cdot \nabla^2 T_{0l}]. \quad (21)$$

The explicit calculation of the above expression in 2D is

$$\begin{aligned} T_l = T_{0l} + \frac{\Delta t}{\rho_{0l} c_{0l}} & \left[ \sum_{k=1}^{iN} \frac{\partial}{\partial p_x} {}_l\psi_k(\mathbf{p}_l) \sum_{n=1}^{iN} {}_l\psi_{kn}^{-1} {}_lk_n \right] \cdot \left[ \sum_{k=1}^{iN} \frac{\partial}{\partial p_x} {}_l\psi_k(\mathbf{p}_l) \sum_{n=1}^{iN} {}_l\psi_{kn}^{-1} T_{0n} \right] \\ & + \frac{\Delta t}{\rho_{0l} c_{0l}} \left[ \sum_{k=1}^{iN} \frac{\partial}{\partial p_y} {}_l\psi_k(\mathbf{p}_l) \sum_{n=1}^{iN} {}_l\psi_{kn}^{-1} {}_lk_n \right] \cdot \left[ \sum_{k=1}^{iN} \frac{\partial}{\partial p_y} {}_l\psi_k(\mathbf{p}_l) \sum_{n=1}^{iN} {}_l\psi_{kn}^{-1} T_{0n} \right] \\ & + \frac{\Delta t k_{0l}}{\rho_{0l} c_{0l}} \left[ \sum_{n=1}^{iN} \frac{\partial^2}{\partial p_x^2} {}_l\psi_k(\mathbf{p}_l) \sum_{n=1}^{iN} {}_l\psi_{kn}^{-1} T_n + \sum_{n=1}^{iN} \frac{\partial^2}{\partial p_y^2} {}_l\psi_k(\mathbf{p}_l) \sum_{n=1}^{iN} {}_l\psi_{kn}^{-1} T_n \right], \end{aligned} \quad (22)$$

where formulas (11) and (12) have been employed. The complete solution procedure follows the below-defined Steps 1–4.

STEP 1. First, the initial conditions are set in the domain and boundary nodes and the required derivatives are calculated from the known nodal values.

STEP 2. Equation (22) is used to calculate the new values of the variable  ${}_lT_n$  at time  $t_0 + \Delta t$  in the domain nodes.

STEP 3. What follows in Steps 3 and 4 defines variable  ${}_lT_n$  at time  $t_0 + \Delta t$  in the Dirichlet, Neumann, and Robin boundary nodes. For this purpose, in Step 3, the coefficients  ${}_l\alpha$  have to be determined from the new values in the domain and from the information on the boundary conditions. Let us introduce domain, Dirichlet, Neumann, and Robin boundary indicators for this purpose. These indicators are defined as

$$\begin{aligned} \Upsilon_{\Omega n} &= \begin{cases} 1, & \mathbf{p}_n \in \Omega, \\ 0, & \mathbf{p}_n \notin \Omega, \end{cases} & \Upsilon_{\Gamma^D}^D &= \begin{cases} 1, & \mathbf{p}_n \in \Gamma^D, \\ 0, & \mathbf{p}_n \notin \Gamma^D, \end{cases} \\ \Upsilon_{\Gamma^N}^N &= \begin{cases} 1, & \mathbf{p}_n \in \Gamma^N, \\ 0, & \mathbf{p}_n \notin \Gamma^N, \end{cases} & \Upsilon_{\Gamma^R}^R &= \begin{cases} 1, & \mathbf{p}_n \in \Gamma^R, \\ 0, & \mathbf{p}_n \notin \Gamma^R. \end{cases} \end{aligned} \quad (23)$$

The coefficients  ${}_l\alpha$  are calculated from the system of linear equations

$$\begin{aligned} & \sum_{k=1}^{{}_lN} {}_l\Upsilon_{\Omega n} {}_l\psi_k({}_l\mathbf{p}_n) {}_l\alpha_k + \sum_{k=1}^{{}_lN} {}_l\Upsilon_{\Gamma^D}^D {}_l\psi_k({}_l\mathbf{p}_n) {}_l\alpha_k \\ & + \sum_{k=1}^{{}_lN} {}_l\Upsilon_{\Gamma^N}^N \frac{\partial}{{}_l\partial n_{\Gamma}} {}_l\psi_k({}_l\mathbf{p}_n) {}_l\alpha_k + \sum_{k=1}^{{}_lN} {}_l\Upsilon_{\Gamma^R}^R \frac{\partial}{{}_l\partial n_{\Gamma}} {}_l\psi_k({}_l\mathbf{p}_n) {}_l\alpha_k \\ & = {}_l\Upsilon_{\Omega n} {}_lT_n + {}_l\Upsilon_{\Gamma^D}^D {}_lT_n^D + {}_l\Upsilon_{\Gamma^N}^N {}_lT_n^N + {}_l\Upsilon_{\Gamma^R}^R {}_lT_n^R \left( \sum_{k=1}^{{}_lN} {}_l\psi_k({}_l\mathbf{p}_n) {}_l\alpha_k - {}_lT_{\Gamma^R \text{ref } n}^R \right). \end{aligned} \quad (24)$$

System (24) can be written in a compact form

$${}_l\Psi {}_l\alpha = {}_l\mathbf{b}, \quad (25)$$

with the following system matrix entries:

$$\begin{aligned} {}_l\Psi_{nk} &= {}_l\Upsilon_{\Omega n} {}_l\psi_k({}_l\mathbf{p}_n) + {}_l\Upsilon_{\Gamma^D}^D {}_l\psi_k({}_l\mathbf{p}_n) \\ & + {}_l\Upsilon_{\Gamma^N}^N \frac{\partial}{{}_l\partial n_{\Gamma}} {}_l\psi_k({}_l\mathbf{p}_n) + {}_l\Upsilon_{\Gamma^R}^R \left[ \frac{\partial}{{}_l\partial n_{\Gamma}} {}_l\psi_k({}_l\mathbf{p}_n) - {}_lT_{\Gamma^R}^R \sum_{k=1}^{{}_lN} {}_l\psi_k({}_l\mathbf{p}_n) \right], \end{aligned} \quad (26)$$

and with the following explicit form of the augmented right-hand side vector:

$${}_lb_n = {}_l\Upsilon_{\Omega n} {}_lT_n + {}_l\Upsilon_{\Gamma^D}^D {}_lT_n^D + {}_l\Upsilon_{\Gamma^N}^N {}_lT_n^N - {}_l\Upsilon_{\Gamma^R}^R {}_lT_{\Gamma^R \text{ref } n}^R. \quad (27)$$

STEP 4. The unknown boundary values are set from equation (7).

The steady-state is achieved when the criterion

$$\max |T_n - T_{0n}| \leq T_{\text{ste}} \quad (28)$$

is satisfied in all computational nodes  $\mathbf{p}_n$ ;  $n = 1, 2, \dots, N$ . The parameter  $T_{\text{ste}}$  is defined as the steady-state convergence margin. In case the steady-state criterion is achieved or the time of calculation exceeds the foreseen time of interest, the calculation is stopped.

## 4. NUMERICAL EXAMPLES

### 4.1. First Test: Boundary Value Problem

The problem is posed on a two-dimensional rectangular domain  $\Omega : p_x^- < p_x < p_x^+, p_y^- < p < y < p_y^+$ , and boundary  $\Gamma_x^- : p_x = p_x^-, p_y^- \leq p_y \leq p_y^+, \Gamma_x^+ : p_x = p_x^+, p_y^- \leq p_y \leq p_y^+, \Gamma_y^- : p_y = p_y^-, p_x^- \leq p_x \leq p_x^+, \Gamma_y^+ : p_y = p_y^+, p_x^- \leq p_x \leq p_x^+$  with  $p_x^- = 0$  m,  $p_x^+ = 0.6$  m,  $p_y^- = 0$  m,  $p_y^+ = 1.0$  m. The material properties are  $\rho = 7850$  kg/m<sup>3</sup>,  $c = 460$  J/kgK, and  $k = 52$  W/mK. The boundary conditions are on the south boundary  $\Gamma_y^-$  of the Dirichlet type with  $T_{\Gamma}^D = 100^\circ\text{C}$ , on the east and north boundaries  $\Gamma_x^+$  and  $\Gamma_y^+$  of the Robin type with  $T_{\Gamma}^R = -h/k$ ,  $h = 750$  W/m<sup>2</sup>K,  $T_{\Gamma}^R = 0^\circ\text{C}$ , and on the west boundary  $\Gamma_x^-$  of the Neumann type with  $T_{\Gamma}^N = 0$  (W/m<sup>2</sup>)/(W/mK). The analytical solution of the test is

$$T_{\text{ana}}(p_x, p_y, t) = 2hT_x^- \sum_{n=1}^{\infty} \frac{\cos \beta_n x [\beta_n \cosh \beta_n (p_y^+ - p_y) + h \sinh \beta_n (p_y^+ - p_y)]}{\cos \beta_n p_x^+ [(\beta_n^2 + h^2) p_x^+ + h] [\beta_n \cosh \beta_n p_y^+ + h \sinh \beta_n p_y^+]}, \quad (29)$$

with  $\beta_n$  representing the positive roots of the equation

$$\beta \tan [\beta (p_x^+ - p_x^-)] = h. \quad (30)$$

This solution represents the NAFEMS benchmark test No. 10 [20]. The solution is in reference [20] given in terms of analytical value for temperature  $T_{\text{NAFEMS}} = 18.25^\circ\text{C}$  at  $p_{\text{NAFEMS } x} = 0.6$  m,  $p_{\text{NAFEMS } y} = 0.2$  m. The rounded eight digit accurate analytical solution used in this paper is  $T_{\text{NAFEMS}} = 18.253756^\circ\text{C}$ . The analytical solution has been calculated also in all computational nodes in order to be able to calculate the error measures that follow. The maximum absolute temperature error  $T_{\text{max}}$  and the average absolute temperature error  $T_{\text{avg}}$  of the numerical solution at time  $t$  are defined as

$$T_{\text{max}} = \max |T(\mathbf{p}_n, t) - T_{\text{ana}}(\mathbf{p}_n, t)|; \quad n = 1, 2, \dots, N, \quad (31)$$

$$T_{\text{avg}} = \sum_{n=1}^N \frac{1}{N} |T(\mathbf{p}_n, t) - T_{\text{ana}}(\mathbf{p}_n, t)|; \quad n = 1, 2, \dots, N, \quad (32)$$

where  $T$  and  $T_{\text{ana}}$  stand for numerical and analytical solution,  $N$  represents the total number of all nodes  $\mathbf{p}_n$  of which first  $N_{\Gamma}$  nodes correspond to the boundary and the remaining  $N_{\Omega}$  to the domain. The node with the maximum temperature error is denoted as  $\mathbf{p}_{\text{max}}$ . The chosen error measures have been made compatible with the studies [21,22].

### 4.2. Computational Parameters and Discussion of the First Test Case

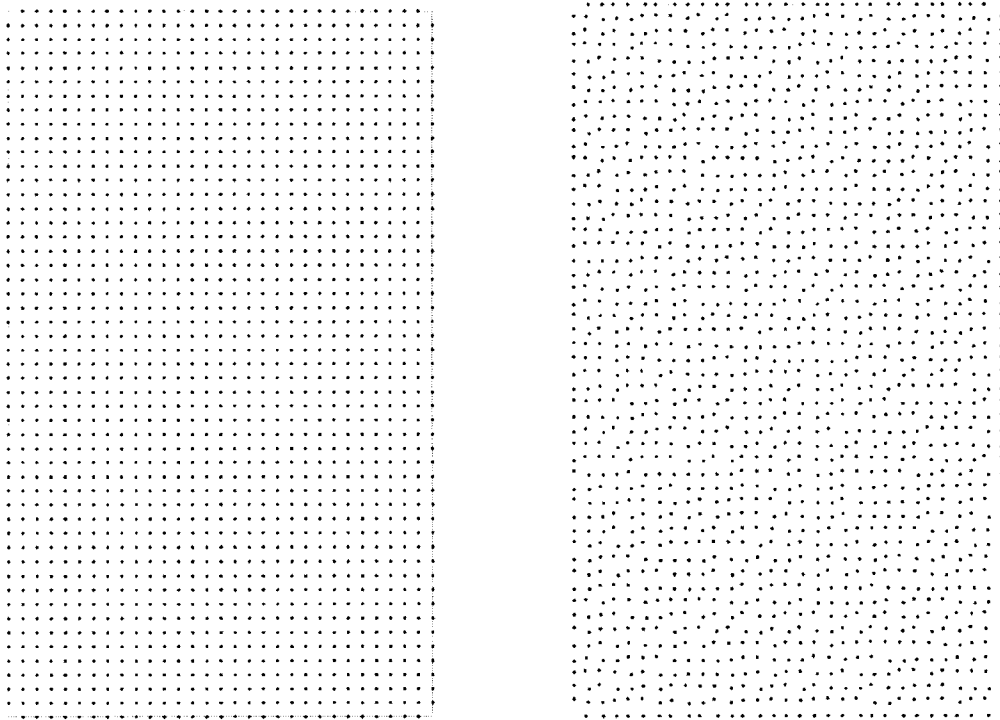
The calculations are performed on three uniform node arrangements  $13 \times 21$  ( $N = 269$ ,  $N_{\Gamma} = 60$ ,  $N_{\Omega} = 209$ ),  $31 \times 51$  ( $N = 1577$ ,  $N_{\Gamma} = 156$ ,  $N_{\Omega} = 1421$ ),  $61 \times 101$  ( $N = 6157$ ,  $N_{\Gamma} = 316$ ,  $N_{\Omega} = 5841$ ), and on the nonuniform node arrangement  $61 \times 101$  ( $N = 6157$ ,  $N_{\Gamma} = 316$ ,  $N_{\Omega} = 5841$ ). A schematic of the uniform node arrangement  $31 \times 51$  is shown in Figure 1a. A randomly displaced nonuniform node arrangement is generated from the uniform node arrangement through transformation

$$p_{n\varsigma} (\text{nonuniform}) = p_{n\varsigma} (\text{uniform}) + c_{\text{random}} \delta r_{\text{min}} p_{n\varsigma} (\text{uniform}); \quad \varsigma = x, y, \quad (33)$$

where  $C_{\text{random}}$  represents a random number  $-1 \leq c_{\text{random}} \leq +1$ ,  $\delta$  represents a displacement factor (in this work fixed to 0.25), and  $r_{\text{min}}$  represents the minimum distance between the two nodes in uniform node arrangement. The boundary nodes are displaced only in the direction perpendicular to the boundary normal. A schematic of the randomly displaced nonuniform node

arrangement  $31 \times 51$  is shown in Figure 1b. The steady state is approached by a transient calculation using a fixed time-step  $\Delta t = 1$  s in regular node arrangements and  $\Delta t = 0.5$  s in irregular node arrangement. The steady state criterion used in all computations is  $T_{\text{ste}} = 10^{-6}^\circ\text{C}$ .

Tables 1–3 show accuracy of the solution as a function of (nonscaled) multiquadrics free parameter  $c$  for different node arrangements and five-noded domain of influence. One can observe the improvement of the accuracy with higher values of  $c$  and denser nodes. One can also observe that in case the value of  $c$  is fixed far from the optimal value (i.e., it takes values 1 or 2) the method does not converge with denser nodes. The solution above  $c = 8$  shows only slight improvement



(a)  $31 \times 51$  uniform node arrangement.

(b)  $31 \times 51$  nonuniform randomly displaced node arrangement

Figure 1.

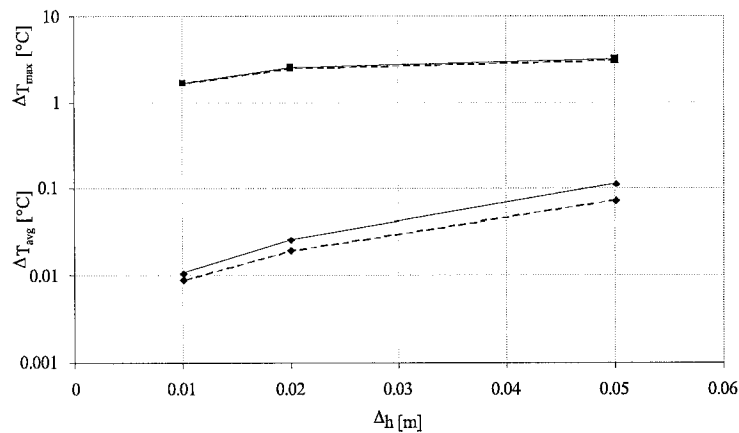


Figure 2. Convergence plot of the maximum error (upper curve) and average error (lower curve) as a function of the minimum node distance for the five-noded support and two multiquadrics parameters. Solid line— $31 \times 51$  node arrangement, dashed line— $61 \times 101$  node arrangement, maximum error ■, average error ♦.

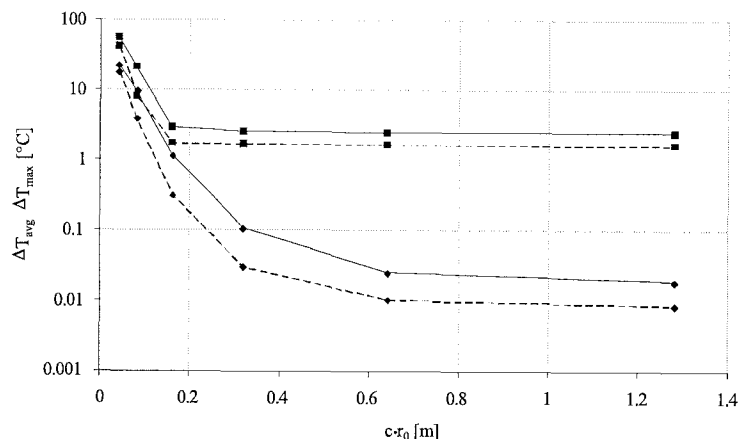


Figure 3. Convergence plot of the maximum error (upper curves) and average error (lower curves) as a function of the multiquadrics parameters for the five-noded support and two node arrangements. Solid line— $31 \times 51$  node arrangement, dashed line— $61 \times 101$  node arrangement, maximum error—■, average error—◆.

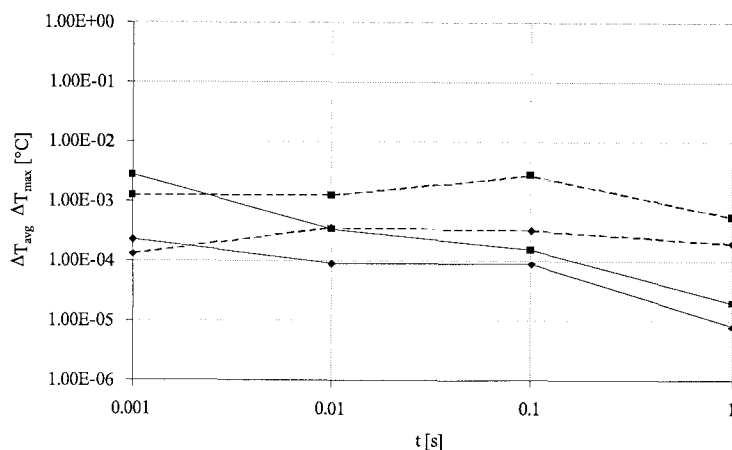


Figure 4. Average and maximum errors as a function of time for the second test case calculated with the FDM and the developed method. Solid line—developed method, dashed line—FDM, maximum error—■, average error—◆.

in maximum error; however the average error can still be significantly improved when changing the parameter  $c$  from 8 to 16. The solution with node arrangement  $13 \times 21$  and  $c = 32$  did not converge. Table 4 shows the same type of information as Table 3, however with the nine-noded domain of influence. In this case the solution with  $c = 16$  and  $c = 32$  did not converge. This result is consistent with the fact that more nodes are used in multiquadrics collocation methods the more the free parameter is restricted to smaller values. Comparison of Tables 3 and 4 shows that better results can be achieved with smaller domain of influence. At the fixed parameter  $c = 8$  the average error is smaller with the smaller domain of influence and the maximum error is smaller with the larger domain of influence.

Next, the calculations are performed on the nonuniform randomly displaced node arrangement. Here, the results did not converge with the five-noded domain of influence. Comparison of Tables 5 and 4 shows the expected degradation of the accuracy with the node arrangement randomisation. Tables 6 and 7 show accuracy of the developed meshfree method in the NAFEMS reference point as compared with the classical FDM. The accuracy of the meshfree method with the uniform  $61 \times 101$  node arrangement and five-noded domain of influence is almost two orders of magnitude higher than with the FDM method structured in the same gridpoints. The error is increased in case of nonuniform node arrangement. However, also in nonuniform case, the error



Table 1. Accuracy of the solution as a function of multiquadrics free parameter  $c$  in terms of average and maximum errors and the position of maximum error for  $13 \times 21$  node arrangement and five-noded domain of influence.

$c$	$\Delta T_{\text{avg}} [^{\circ}\text{C}]$	$\Delta T_{\text{max}} [^{\circ}\text{C}]$	$p_{\text{max } x} [\text{m}]$	$p_{\text{max } y} [\text{m}]$
1	12.8558	29.9918	0.0000	0.3000
2	2.6133	5.5789	0.0000	0.3500
4	0.3114	3.4979	0.6000	0.0500
8	0.0891	3.1707	0.6000	0.0500
16	0.0719	3.0920	0.6000	0.0500
32	div			

Table 2. Accuracy of the solution as a function of multiquadrics free parameter  $c$  in terms of average and maximum errors and the position of maximum error for  $31 \times 51$  node arrangement and five-noded domain of influence.

$c$	$\Delta T_{\text{avg}} [^{\circ}\text{C}]$	$\Delta T_{\text{max}} [^{\circ}\text{C}]$	$p_{\text{max } x} [\text{m}]$	$p_{\text{max } y} [\text{m}]$
1	23.0263	57.0299	0.0000	0.2000
2	9.8407	21.5167	0.0000	0.3200
4	1.1828	2.9379	0.6000	0.0200
8	0.1087	2.5910	0.6000	0.2000
16	0.0261	2.5172	0.6000	0.2000
32	0.0196	2.4996	0.6000	0.2000

Table 3. Accuracy of the solution as a function of multiquadrics free parameter  $c$  in terms of average and maximum errors and the position of maximum error for  $61 \times 101$  node arrangement and five-noded domain of influence.

$c$	$\Delta T_{\text{avg}} [^{\circ}\text{C}]$	$\Delta T_{\text{max}} [^{\circ}\text{C}]$	$p_{\text{max } x} [\text{m}]$	$p_{\text{max } y} [\text{m}]$
1	27.8036	72.9256	0.0000	0.1300
2	18.5475	42.4449	0.0000	0.2500
4	3.9476	8.3054	0.0000	0.3500
8	0.3210	1.7675	0.6000	0.0100
16	0.0314	1.7042	0.6000	0.0100
32	0.0107	1.6903	0.6000	0.0100

Table 4. Accuracy of the solution as a function of multiquadrics free parameter  $c$  in terms of average and maximum error and the position of maximum error for  $61 \times 101$  node arrangement and nine-noded domain of influence.

$c$	$\Delta T_{\text{avg}} [^{\circ}\text{C}]$	$\Delta T_{\text{max}} [^{\circ}\text{C}]$	$p_{\text{max } x} [\text{m}]$	$p_{\text{max } y} [\text{m}]$
1	21.3924	50.4141	0.0000	0.2200
2	7.0673	15.0366	0.0000	0.3300
4	0.6918	1.4331	0.0000	0.3700
8	0.0704	0.8284	0.6000	0.0100
16	div			
32	div			

Table 5. Accuracy of the solution as a function of multiquadrics free parameter  $c$  in terms of average and maximum error and the position of maximum error for  $61 \times 101$  nonuniform node arrangement and nine-noded domain of influence.

$c$	$\Delta T_{\text{avg}} [^{\circ}\text{C}]$	$\Delta T_{\text{max}} [^{\circ}\text{C}]$	$p_{\text{max } x} [\text{m}]$	$p_{\text{max } y} [\text{m}]$
1	22.5573	53.1913	0.0000	0.2113
2	9.3926	20.0383	0.0000	0.3191
4	1.2326	2.5587	0.0000	0.3897
5	0.5637	1.1684	0.0000	0.3897
16	div			
32	div			

Table 6. Accuracy of the solution in NAFEMS reference point  $\mathbf{p}_{\text{NAFEMS}}$  as a function grid density at fixed multiquadrics free parameter for different node arrangements and five- and nine-noded domains of influence.

Grid	Support	$c$	$T [^{\circ}\text{C}]$	$T - T_{\text{NAFEMS}} [^{\circ}\text{C}]$
$13 \times 21$	5	16	18.3613	0.1075
$31 \times 51$	5	32	18.2855	0.0317
$61 \times 101$	5	32	18.2594	0.0056
$61 \times 101$ (uniform)	9	8	18.2512	-0.0026
$61 \times 101$ (nonuniform)	9	5	18.0395	0.2143

Table 7. Accuracy of the classical FDM solution in NAFEMS reference point as a function of regular grid density.

Grid	$T [^{\circ}\text{C}]$	$T - T_{\text{NAFEMS}} [^{\circ}\text{C}]$
$61 \times 101$	17.9827	-0.2711
$121 \times 201$	18.1074	-0.1464
$241 \times 401$	18.1754	-0.0783

in the reference point is only  $0.2143^{\circ}\text{C}$  (i.e., in the permille range) compared to the characteristic problem temperature difference of  $100^{\circ}\text{C}$ .

#### 4.3. Second Test: Initial Value Problem

The geometry of the problem is formally posed on a similar region as the first test case; however the region is square with  $p_x^- = 0 \text{ m}$ ,  $p_x^+ = 1.0 \text{ m}$ ,  $p_y^- = 0 \text{ m}$ ,  $p_y^+ = 1.0 \text{ m}$ . The material properties are set to unit values  $\rho = 1 \text{ kg/m}^3$ ,  $c = 1 \text{ J/kgK}$ ,  $k = 1 \text{ W/mK}$ . Boundary conditions on the east  $\Gamma_x^+$  and north boundaries  $\Gamma_y^+$  are of the Dirichlet type with  $T_{\Gamma}^D = 0^{\circ}\text{C}$ , and on the west  $\Gamma_x^-$  and south boundaries  $\Gamma_y^-$  are of the Neumann type with  $T_{\Gamma}^N = 0 \text{ (W/m}^2\text{)}/\text{W/mK}$ .

The initial conditions are  $T_0 = 1^{\circ}\text{C}$ . The analytical solution [23] of the test is

$$T_{\text{ana}}(p_x, p_y, t) = T_{\text{ana}}(p_x, t)T_{\text{ana}}(p_y, t) \quad (34)$$

with

$$T_{\text{ana}}(p_{\zeta}, t) = \frac{4}{\pi} \sum_{n=1}^{\infty} \frac{-1^n}{2n+1} \exp \left[ -\frac{k(2n+1)^2 \pi^2 t}{4\rho c (p_{\zeta}^+ - p_{\zeta}^-)^2} \right] \cos \left[ \frac{(2n+1)\pi(p_{\zeta} - 1)}{2(p_{\zeta}^+ - p_{\zeta}^-)} \right]; \quad \zeta = x, y. \quad (35)$$

#### 4.4. Computational Parameters and Discussion of the Second Test Case

The calculations are performed on four different uniform node arrangements  $11 \times 11$  ( $N = 117$ ,  $N_{\Gamma} = 36$ ,  $N_{\Omega} = 81$ ),  $21 \times 21$  ( $N = 437$ ,  $N_{\Gamma} = 76$ ,  $N_{\Omega} = 361$ ),  $41 \times 41$  ( $N = 1677$ ,  $N_{\Gamma} = 156$ ,  $N_{\Omega} = 1521$ ),  $101 \times 101$  ( $N = 10197$ ,  $N_{\Gamma} = 396$ ,  $N_{\Omega} = 9801$ ), and five-noded domain of influence, respectively. The timesteps  $\Delta t = 10^{-4}$  s and  $\Delta t = 10^{-5}$  s are used in the calculations with  $41 \times 41$  node arrangement. The accuracy of the method is assessed in terms of the maximum and average errors at times  $t = 0.001$  s,  $t = 0.01$  s,  $t = 0.1$  s, and  $t = 1.0$  s.

Tables 8–10 show accuracy of the solution as a function of multiquadrics free parameter  $c$  for different grid arrangements and five-noded support. One can observe the improvement of the

Table 8. Accuracy of the solution as a function of multiquadrics free parameter  $c$  at times  $t = 0.001$  s,  $t = 0.01$  s,  $t = 0.1$  s, and  $t = 1.0$  s in terms of average error, maximum error, and the position of the maximum error for  $11 \times 11$  node arrangement with five-noded domain of influence and  $\Delta t = 10^{-4}$  s.

$t$ [s]	$c$	$\Delta T_{\text{avg}}$ [°C]	$\Delta T_{\text{max}}$ [°C]	$p_{\text{max } x}$ [m]	$p_{\text{max } y}$ [m]
0.001	8	1.184E-2	1.259E-1	0.900	0.900
0.001	16	1.182E-2	1.255E-1	0.900	0.900
0.001	32	1.181E-2	1.254E-1	0.900	0.900
0.01	8	4.862E-3	2.286E-2	0.700	0.700
0.01	16	4.767E-3	2.245E-2	0.700	0.700
0.01	32	4.746E-3	2.235E-2	0.700	0.700
0.1	8	1.242E-3	3.471E-3	0.200	0.200
0.1	16	7.139E-4	2.592E-3	0.200	0.200
0.1	32	6.239E-4	2.403E-3	0.200	0.200
1.0	8	6.997E-5	1.792E-4	0.100	0.100
1.0	16	9.068E-6	2.818E-5	0.100	0.100
1.0	32	4.681E-6	1.120E-5	0.300	0.000

Table 9. Accuracy of the solution as a function of multiquadrics free parameter  $c$  at times  $t = 0.001$  s,  $t = 0.01$  s,  $t = 0.1$  s, and  $t = 1.0$  s in terms of average error, maximum error, and the position of the maximum error for  $21 \times 21$  node arrangement with five-noded domain of influence and  $\Delta t = 10^{-4}$  s.

$t$ [s]	$c$	$\Delta T_{\text{avg}}$ [°C]	$\Delta T_{\text{max}}$ [°C]	$p_{\text{max } x}$ [m]	$p_{\text{max } y}$ [m]
0.001	8	4.593E-3	4.413E-2	0.900	0.900
0.001	16	4.527E-3	4.377E-2	0.900	0.900
0.001	32	4.512E-3	4.368E-2	0.900	0.900
0.01	8	1.574E-3	7.121E-3	0.750	0.750
0.01	16	1.329E-3	6.421E-3	0.750	0.750
0.01	32	1.282E-3	6.255E-3	0.750	0.750
0.1	8	1.241E-3	2.387E-3	0.200	0.200
0.1	16	4.344E-4	1.032E-3	0.150	0.150
0.1	32	2.868E-4	8.154E-4	0.150	0.150
1.0	8	1.071E-4	2.695E-4	0.050	0.050
1.0	16	2.046E-5	5.262E-5	0.050	0.050
1.0	32	4.730E-6	1.337E-5	0.050	0.050

Table 10. Accuracy of the solution as a function of multiquadrics free parameter  $c$  at times  $t = 0.001$  s,  $t = 0.01$  s,  $t = 0.1$  s, and  $t = 1.0$  s in terms of average error, maximum error, and the position of the maximum error for  $41 \times 41$  node arrangement with five-noded domain of influence and  $\Delta t = 10^{-4}$  s.

$t$ [s]	$c$	$\Delta T_{\text{avg}}$ [°C]	$\Delta T_{\text{max}}$ [°C]	$p_{\text{max } x}$ [m]	$p_{\text{max } y}$ [m]
0.001	8	1.798E-3	2.405E-2	0.950	0.950
0.001	16	1.699E-3	2.319E-2	0.950	0.950
0.001	32	1.679E-3	2.298E-2	0.950	0.950
0.01	8	1.033E-3	3.678E-3	0.825	0.825
0.01	16	6.092E-4	2.647E-3	0.825	0.825
0.01	32	5.415E-4	2.418E-3	0.825	0.825
0.1	8	2.036E-3	3.761E-3	0.025	0.025
0.1	16	3.815E-4	6.548E-4	0.400	0.400
0.1	32	1.815E-4	3.200E-4	0.450	0.450
1.0	8	2.113E-4	5.277E-4	0.025	0.025
1.0	16	3.115E-5	7.810E-5	0.025	0.025
1.0	32	9.160E-6	2.332E-5	0.025	0.025

Table 11. Accuracy of the solution as a function of multiquadrics free parameter  $c$  at times  $t = 0.001$  s,  $t = 0.01$  s,  $t = 0.1$  s, and  $t = 1.0$  s in terms of average error, maximum error, and the position of the maximum error for  $41 \times 41$  node arrangement with five-noded domain of influence and  $\Delta t = 10^{-5}$  s.

$t$ [s]	$c$	$\Delta T_{\text{avg}}$ [°C]	$\Delta T_{\text{max}}$ [°C]	$p_{\text{max } x}$ [m]	$p_{\text{max } y}$ [m]
0.001	8	1.239E-3	1.571E-2	0.925	0.925
0.001	16	1.179E-3	1.502E-2	0.925	0.925
0.001	32	1.168E-3	1.485E-2	0.925	0.925
0.01	8	8.092E-4	2.641E-3	0.250	0.250
0.01	16	3.828E-4	1.772E-3	0.275	0.275
0.01	32	3.332E-4	1.623E-3	0.275	0.275
0.1	8	1.969E-3	3.864E-3	0.975	0.975
0.1	16	3.155E-4	6.328E-4	0.900	0.900
0.1	32	1.098E-4	3.037E-4	0.925	0.925
1.0	8	2.065E-4	5.152E-4	0.025	0.025
1.0	16	2.619E-5	6.539E-5	0.025	0.025
1.0	32	4.191E-6	1.058E-5	0.025	0.025

accuracy with higher values of  $c$  and denser node arrangement. Comparison of Tables 10 and 11 shows expected convergence properties of the method, that better results can be achieved with reduction of the timestep from  $\Delta t = 10^{-4}$  s to  $\Delta t = 10^{-5}$  s. Information in Tables 12 and 13 shows similar accuracy of the developed meshless method as compared with the classical FDM at shorter times  $t = 0.001$  s and  $t = 0.01$  s immediately after the abrupt boundary conditions jump, and an order of magnitude better accuracy at longer transient times  $t = 0.1$  s and  $t = 1.0$  s. The method is unstable with the timestep  $\Delta t = 10^{-3}$  s because of the explicit approach.

Both test cases show that the accuracy of the method monotonically increases with larger value of  $c$ . Because of the lack of the suitable theory for determining the proper value of the free parameter one can confidently use the highest values of  $c$  which give convergence.

Table 12. Accuracy of the solution at times  $t = 0.001\text{ s}$ ,  $t = 0.01\text{ s}$ ,  $t = 0.1\text{ s}$ , and  $t = 1.0\text{ s}$  in terms of average and maximum errors and the position of maximum error for  $101 \times 101$  node arrangement, five-noded domain of influence, fixed multiquadrics free parameter  $c = 32$  and  $\Delta t = 10^{-5}\text{ s}$ .

$t$ [s]	$c$	$\Delta T_{\text{avg}}$ [ $^{\circ}\text{C}$ ]	$\Delta T_{\text{max}}$ [ $^{\circ}\text{C}$ ]	$p_{\text{max } x}$ [m]	$p_{\text{max } y}$ [m]
0.001	32	2.352E-4	2.809E-3	0.940	0.940
0.01	32	9.371E-5	3.523E-4	0.800	0.800
0.1	32	9.243E-5	1.582E-4	0.270	0.270
1.0	32	8.324E-6	2.066E-5	0.010	0.010

Table 13. Accuracy of the FDM solution at times  $t = 0.001\text{ s}$ ,  $t = 0.01\text{ s}$ ,  $t = 0.1\text{ s}$ , and  $t = 1.0\text{ s}$  in terms of average and maximum errors and the position of maximum error for  $101 \times 101$  regular grid and  $\Delta t = 10^{-5}\text{ s}$ .

$t$ [s]	$\Delta t$ [s]	$\Delta T_{\text{avg}}$ [ $^{\circ}\text{C}$ ]	$\Delta T_{\text{max}}$ [ $^{\circ}\text{C}$ ]	$p_{\text{max } x}$ [m]	$p_{\text{max } y}$ [m]
0.001	1.0E-5	1.368E-4	1.273E-3	0.925	0.950
0.01	1.0E-5	3.722E-4	1.298E-3	0.020	0.890
0.1	1.0E-5	3.363E-4	2.786E-3	0.000	0.010
1.0	1.0E-5	2.029E-4	5.649E-4	0.000	0.010

## 5. CONCLUSIONS

This paper represents a new (very) simple meshfree formulation for solving a wide range of diffusion problems. The numerical tests show much higher accuracy of the developed method as compared with the classical FDM. The only exception observed is the solution at short times immediately after the Dirichlet jump where similar numerical approximation properties are observed. The time-marching is performed in a simple explicit way. The governing equation is solved in its strong form. No polygonisation and integrations are needed. The developed method is almost independent of the problem dimension. The complicated geometry can easily be coped with. The method appears efficient, because it does not require a solution of a large system of equations like the original Kansa method. Instead, small systems of linear equations have to be solved in each timestep for each node and associated domain of influence, probably representing the most natural and automatic domain decomposition. This feature of the developed method represents its principal difference from the other related local approaches, where the resultant matrix is large and sparse [15,17–19]. The method is simple to learn and simple to code. The method can cope with very large problems since the computational effort grows approximately linear with the number of the nodes. The developments in this paper can be straightforwardly extended to tackle other types of partial differential equations. Our ongoing research is focused on the extension of the method to implicit time-marching which might overcome the inherent stability problem of the explicit approach.

## REFERENCES

1. S.N. Atluri and S. Shen, *The Meshless Method*, Tech Science Press, Forsyth, (2002).
2. G.R. Liu, *Mesh Free Methods*, CRC Press, Boca Raton, FL, (2003).
3. S.N. Atluri, *The Meshless Method for Domain and BIE Discretisations*, Tech Science Press, Forsyth, (2004).
4. B. Šarler, Chapter 9: “Meshless Methods”, In *Advanced Numerical Methods in Heat Transfer*, (Edited by A.J. Nowak), pp. 225–247, Silesian Technical University Press, Gliwice, (2004).
5. M.D. Buhmann, *Radial Basis Function: Theory and Implementations*, Cambridge University Press, Cambridge, (2003).
6. E.J. Kansa, Multiquadrics—A scattered data approximation scheme with applications to computational fluid dynamics—II. Solutions to parabolic, hyperbolic and elliptic partial differential equations, *Computers Math. Applic.* **19**, 147–161, (1990).

7. G.E. Fasshauer, Solving partial differential equations by collocation with radial basis functions, In *Surface Fitting and Multiresolution Methods*, (Edited by A.L. Mehaute, C. Rabut and L.L. Schumaker), pp. 131–138, (1997).
8. H. Power and W.A. Barraco, Comparison analysis between unsymmetric and symmetric RBFCMs for the numerical solution of PDEs, *Computers Math. Applic.* **43** (3–5), 551–583, (2002).
9. W. Chen, New RBF collocation schemes and kernel RBFs with applications, *Lecture Notes in Computational Science and Engineering* **26**, 75–86, (2002).
10. N. Mai-Duy and T. Tran-Cong, Indirect RBFN method with thin plate splines for numerical solution of differential equations, *Computer Modeling in Engineering & Sciences* **4**, 85–102, (2003).
11. B. Šarler, A radial basis function collocation approach in computational fluid dynamics, *Computer Modeling in Engineering & Sciences* **7**, 185–194, (2005).
12. N. Mai-Duy and T. Tran-Cong, Numerical solution of Navier-Stokes equations using multiquadric radial basis function networks, *Neural Networks* **14**, 185–199, (2001).
13. B. Šarler, J. Perko and C.S. Chen, Radial basis function collocation method solution of natural convection in porous media, *Int. J. Numer. Methods Heat & Fluid Flow* **14**, 187–212, (2004).
14. I. Kovačević, A. Poredoš and B. Šarler, Solving the Stefan problem by the RBFCM, *Numer. Heat Transfer, Part B: Fundamentals* **44**, 1–24, (2003).
15. C.S. Chen, M. Ganesh, M.A. Golberg and A.H.-D. Cheng, Multilevel compact radial basis functions based computational scheme for some elliptic problems, *Computers Math. Applic.* **43** (3–5), 359–378, (2002).
16. N. Mai-Duy and T. Tran-Cong, Mesh-free radial basis function network methods with domain decomposition for approximation of functions and numerical solution of Poisson's equations, *Engineering Analysis with Boundary Elements* **26**, 133–156, (2002).
17. C.K. Lee, X. Liu and S.C. Fan, Local multiquadric approximation for solving boundary value problems, *Computational Mechanics* **30**, 395–409, (2003).
18. A.I. Tolstykh and D.A. Shirobokov, On using radial basis functions in a “finite difference” mode with applications to elasticity problems, *Computational Mechanics* **33**, 68–79, (2003).
19. C. Shu, H. Ding and K.S. Yeo, Local radial basis function-based differential quadrature method and its application to solve two-dimensional incompressible Navier-Stokes equations, *Computer Methods in Applied Mechanics and Engineering* **192**, 941–954, (2003).
20. A.D. Cameron, J.A. Casey and G.B. Simpson, *Benchmark Tests for Thermal Analysis*, NAFEMS National Agency for Finite Element Methods & Standards, Department of Trade and Industry, National Engineering Laboratory, Glasgow, (1986).
21. A.J. Dalhuijsen and A. Segal, Comparison of finite element techniques for solidification problems, *International Journal for Numerical Methods in Engineering* **29**, 1807–1829, (1986).
22. B. Šarler and G. Kuhn, Dual reciprocity boundary element method for convective-diffusive solid-liquid phase change problems, Part 2: Numerical examples, *Engineering Analysis with Boundary Elements* **21**, 65–79, (1998).
23. H.S. Carslaw and J.C. Jaeger, *Conduction of Heat in Solids*, Second edition, Clarendon Press, Oxford, (1995).